IPEM
Institute of Physics and
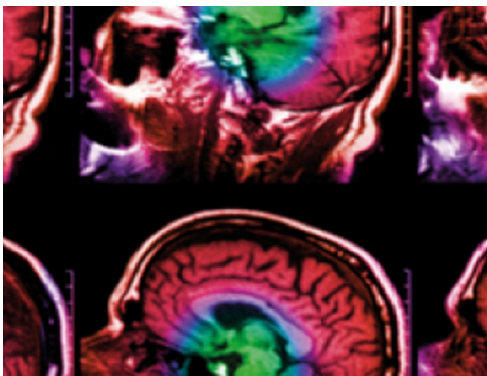Engineering in Medicine

PAPER

Full-volume three-component intraventricular vector flow mapping by triplane color Doppler

To cite this article: Florian Vixège *et al* 2022 *Phys. Med. Biol.* **67** 095004

View the article online for updates and enhancements.

IPEM | IOP

Series in Physics and Engineering in Medicine and Biology

Your publishing choice in medical physics, biomedical engineering and related subjects.

Start exploring the collection–download the first chapter of every title for free.

Physics in Medicine & Biology

IPEM
Institute of Physics and
Engineering in Medicine

CrossMark

PAPER

Full-volume three-component intraventricular vector flow mapping by triplane color Doppler

Florian Vixège[1], Alain Berod[2], Pierre-Yves Courand[1,3], Simon Mendez[2] , Franck Nicoud[2],
Philippe Blanc-Benon[4], Didier Vray[1] and Damien Garcia[1,*]

1. CREATIS UMR 5220, U1294, University Lyon 1, INSA Lyon, France
2. IMAG UMR 5149, University of Montpellier, France
3. Department of Echocardiography, Croix-Rousse Hospital, Lyon, France
4. École Centrale de Lyon, LMFA UMR 5509, University Lyon, France
* Author to whom any correspondence should be addressed.

E-mail: Florian.Vixege@creatis.insa-lyon.fr, Garcia.Damien@gmail.com and Damien.Garcia@inserm.fr

Abstract

Objective. Intraventricular vector flow mapping (iVFM) is a velocimetric technique for retrieving two-dimensional velocity vector fields of blood flow in the left ventricular cavity. This method is based on conventional color Doppler imaging, which makes iVFM compatible with the clinical setting. We have generalized the iVFM for a three-dimensional reconstruction (3D-iVFM). *Approach.* 3D-iVFM is able to recover three-component velocity vector fields in a full intraventricular volume by using a clinical echocardiographic triplane mode. The 3D-iVFM problem was written in the spherical (radial, polar, azimuthal) coordinate system associated to the six half-planes produced by the triplane mode. As with the 2D version, the method is based on the mass conservation, and free-slip boundary conditions on the endocardial wall. These mechanical constraints were imposed in a least-squares minimization problem that was solved through the method of Lagrange multipliers. We validated 3D-iVFM *in silico* in a patient-specific CFD (computational fluid dynamics) model of cardiac flow and tested its clinical feasibility *in vivo* in patients and in one volunteer. *Main results.* The radial and polar components of the velocity were recovered satisfactorily in the CFD setup (correlation coefficients, $r = 0.99$ and 0.78). The azimuthal components were estimated with larger errors ($r = 0.57$) as only six samples were available in this direction. In both *in silico* and *in vivo* investigations, the dynamics of the intraventricular vortex that forms during diastole was deciphered by 3D-iVFM. In particular, the CFD results showed that the mean vorticity can be estimated accurately by 3D-iVFM. *Significance.* Our results tend to indicate that 3D-iVFM could provide full-volume echocardiographic information on left intraventricular hemodynamics from the clinical modality of triplane color Doppler.

1. Introduction

During diastole, blood from the left atrium flows into the left ventricle through the mitral valve. A large vortex (swirling motion) is formed and covers most of the intraventricular cavity (Charonko *et al* 2013, Bermejo *et al* 2015). When left ventricular filling is impaired (diastolic dysfunction), a change in blood flow occurs, with a significant impact on intracardiac vortices. There is indeed a physiological link between the vortex and the healthy heart, which seems to be disturbed in patients with heart failure. It thus appears that the left intraventricular vortex is a key mechanical biomarker of cardiac function (Gharib *et al* 2006, Hendabadi *et al* 2013, Arvidsson *et al* 2016). For example, Martínez-Legazpi *et al* showed by color Doppler echocardiography that the vortical flow has a decreased contribution to filling volume in patients with hypertrophic cardiomyopathy, whereas it is increased in patients with nonischemic dilated cardiomyopathy (Martínez-

Legazpi *et al* 2014). Using cardiac magnetic resonance, Töger *et al* reported that the fraction of left ventricular volume occupied by the vortex ring during diastasis is decreased in patients with heart failure (Töger *et al* 2016). Marchese *et al* observed via high-frame-rate blood speckle tracking that left ventricular volume and pressure overload in children with congenital heart disease affect the location of the vortex in the left ventricle (Marchese *et al* 2021). Given the novelty of interest in the intraventricular vortex for the assessment of cardiac function, there is not yet a consensus on the choice of imaging technique and biomechanical indices. Nevertheless, the recent works warrant further investigations of intraventricular vortical dynamics as a marker of diastolic dysfunction.

The characterization of this intraventricular vortex can be performed under the condition that an intracardiac velocity vector field is available. Two commonly used imaging techniques for the assessment of the intracardiac blood flow in a clinical setting are CMR (cardiac magnetic resonance) and echocardiography. CMR allows the clinician to collect 4D (3D + time) information of the flow, from acquisitions on a few consecutive cardiac cycles with prospective gating. Its operating time, from 30 min to 60 min per patient, as well as the examination costs, make it a solution primarily intended for clinical research (Eriksson *et al* 2010, Markl *et al* 2016). In contrast, Doppler echocardiography is a widely used clinical modality for blood flow analyses. Doppler echocardiography, in its most classical version, yields only one component of the velocity vectors (Jensen *et al* 2016), the one parallel to the direction of the ultrasound wave. To overcome this limitation, several ultrasound imaging techniques have been developed for a 2D vector depiction of the intracardiac flow, such as echo-PIV (echographic particle image velocimetry) by contrast-enhanced echocardiography (Kheradvar *et al* 2010, Chen *et al* 2021), blood speckle tracking (Fadnes *et al* 2014, Daae *et al* 2021), or *i*VFM (intraventricular vector flow mapping) (Garcia *et al* 2010, Assi *et al* 2017). The echo-PIV technique requires the intravenous injection of microbubbles, which is not compatible with a routine clinical use. Blood speckle tracking has the advantage of being free of microbubbles and uses ultrasound signals backscattered by red blood cells (Garcia *et al* 2017, Daae *et al* 2021). Sensitive to the clutter signals, this technique nevertheless seems well adapted to pediatric echocardiography where spatial resolution is higher than in adults (Nyrnes *et al* 2020).

To get a broader view of the heart circulation and to overcome the clinical limitations of 3D CMR velocimetry, some research groups have also focused on 3D reconstruction of intracardiac flows by ultrasound. Some of the methods used were derived from 2D techniques. Feasibility of echo-PIV to obtain a volumetric view of intraventricular flow has been described *in vitro* and *in vivo* (Sengupta *et al* 2012, Voorneveld *et al* 2020, Chen *et al* 2021). Gomez *et al* recovered the 3D flow (Gomez *et al* 2013, 2015) by spatio-temporally registering three or four color Doppler volumes acquired from different acoustic windows. These two approaches cannot be used routinely for clinical purposes because of their methodological constraints (microbubbles, multi-view). Inspired by 2D *i*VFM, Grønli *et al* reconstructed 3D intraventricular flow from Doppler volumes with an optimization method that aimed to conserve the mass (continuity equation) and momentum (Navier–Stokes equations). In this study, the intracardiac pressure gradients were omitted in the Navier–Stokes equations to simplify the numerical problem. After writing the velocity fields with B-splines, the problem was solved using the open-source package TensorFlow (Grønli *et al* 2018). Although closer to the clinical situation, it remains difficult to rely on Doppler volumes because of their low temporal resolution.

To obtain a three-dimensional outlook of the left intraventricular flow, we hypothesized that our 2D *i*VFM algorithm (Assi *et al* 2017, Vixège *et al* 2021b) could be generalized to 3D by using the triplane mode available on clinical ultrasound scanners. Triplane imaging is a mode that has been made available in clinical scanners since the 1990s. Triplane echocardiography allows acquisition of three planes from the same heartbeat, with relatively high temporal and spatial resolutions. When the ultrasound matrix array is placed in the apical window, 2-, 3-, and 4-chamber long-axis views are displayed with 60 degree interplane angles (figure 1). A clinical analysis based on triplane imaging is an alternative when the volume echocardiographic technique is not feasible (e.g. insufficient resolution). The triplane mode has indeed shown clinical relevance in echocardiography laboratories. For example, its diagnostic advantages have been evaluated in the calculation of ejection fraction (Malm *et al* 2006, Nucifora *et al* 2009), and global longitudinal strain by speckle-tracking (Onishi *et al* 2015). From these studies, it appears that these three planes contain sufficient information for an accurate analysis of the global volume and deformations of the left ventricle. In the same vein, we postulated that the Doppler velocities of these three planes also contain sufficient information for an adequate construction of the three-dimensional intraventricular flow. This would be an advantage over volume Doppler as triplane color Doppler provides a higher imaging rate.

In this paper, we introduce a 3D *i*VFM technique based on triplane Doppler-echo, which generalizes the 2D *i*VFM developed by Assi *et al* (2017) and Vixège *et al* (2021b). An incomplete version was briefly presented in a proceeding (Vixège *et al* 2021a). The 3D-*i*VFM approach allows the echographer to estimate the 3D intraventricular flow from three color-Doppler planes, by using a minimization problem constrained by hemodynamic properties (mass conservation in the cardiac cavity, and free-slip boundary conditions on the endocardium). The physical equality constraints were imposed using the Lagrange multiplier method. The
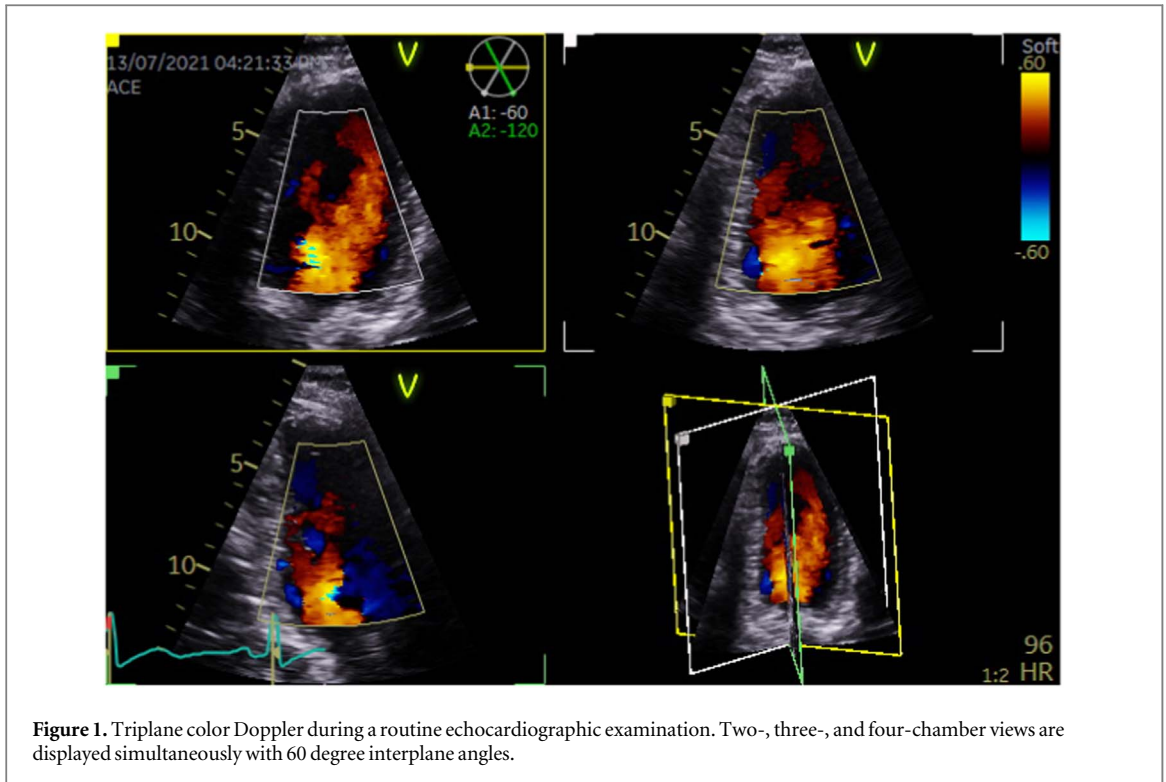
Figure 1. Triplane color Doppler during a routine echocardiographic examination. Two-, three-, and four-chamber views are displayed simultaneously with 60 degree interplane angles.

regularization parameter that controls the smoothing was determined automatically through the *L*-curve method. In the following, we describe the 3D-*i*VFM method and its numerical formulation, its validation using a patient-specific CFD (computational fluid dynamics) model, and its clinical applicability through *in vivo* examples.

2. Methods
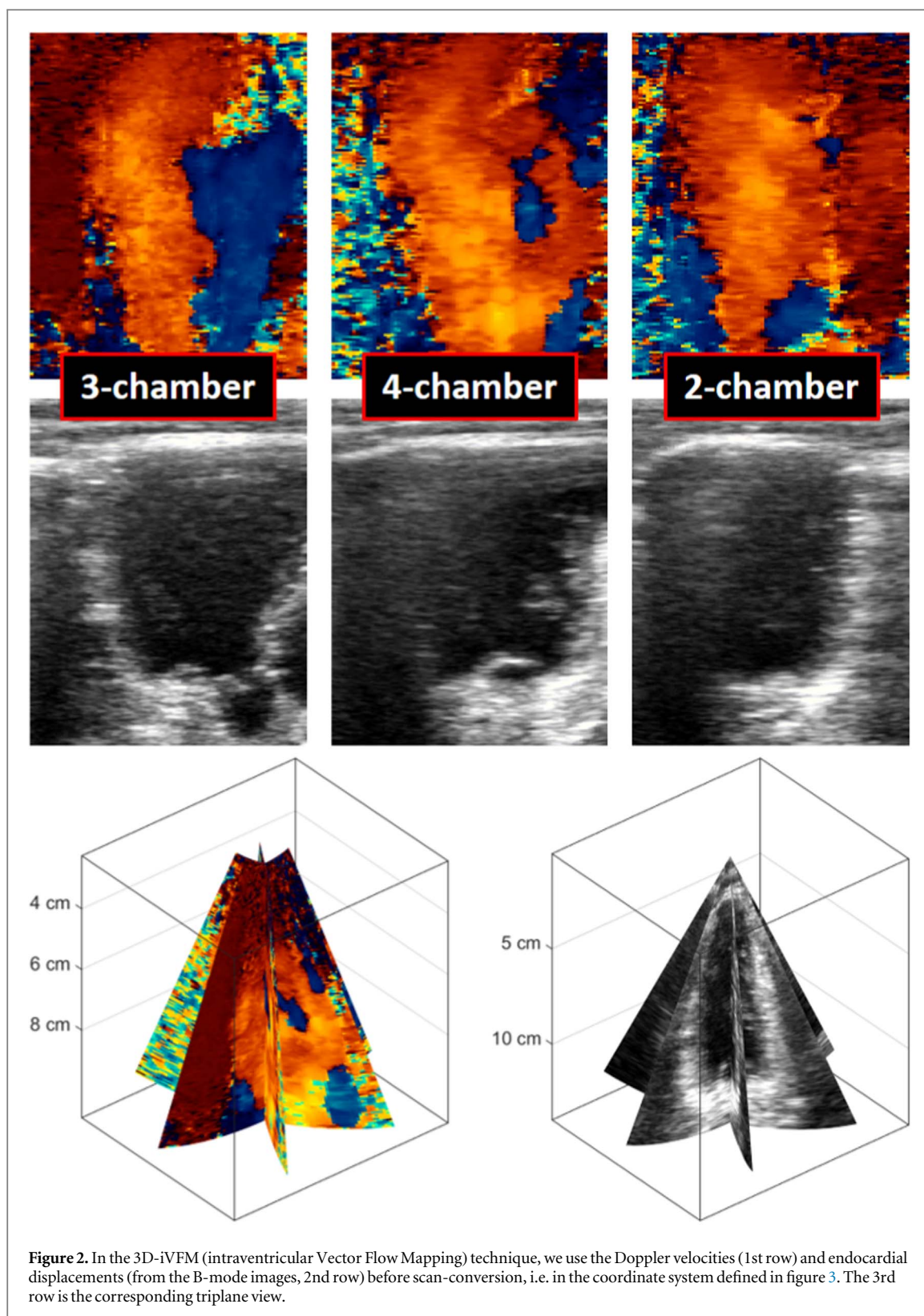
2.1. Triplane echocardiographic mode

The objective of 3D-*i*VFM (3D-*intraventricular* Vector Flow Mapping) is to recover full-volume three-component velocity fields, in the left ventricular cavity, by using triplane color Doppler. Figure 1 illustrates a triplane color Doppler, which provides Doppler velocities from three different apical long-axis views separated by a 60° angle: the two-chamber, three-chamber, and four-chamber views. We chose the triplane mode (rather than volume Doppler) because (1) the ultrasound data before scan-conversion are available (figure 2) through the workstation EchoPAC (GE Healthcare), and (2) the temporal resolution is higher. The EchoPAC software gives access to the series of three planes that contain both Doppler velocities and 8 bit B-mode images in the spherical coordinate system $\{r, \theta, \varphi\}$ related to the cardiac phased array (figure 3). In this spherical system, $r \geqslant 0$, $\theta \in [0, \pi/2]$, and $\varphi \in [0, 2\pi]$. Figure 2 shows a triplane B-mode+Doppler data from which a full-volume vector flow is reconstructed by 3D-*i*VFM.

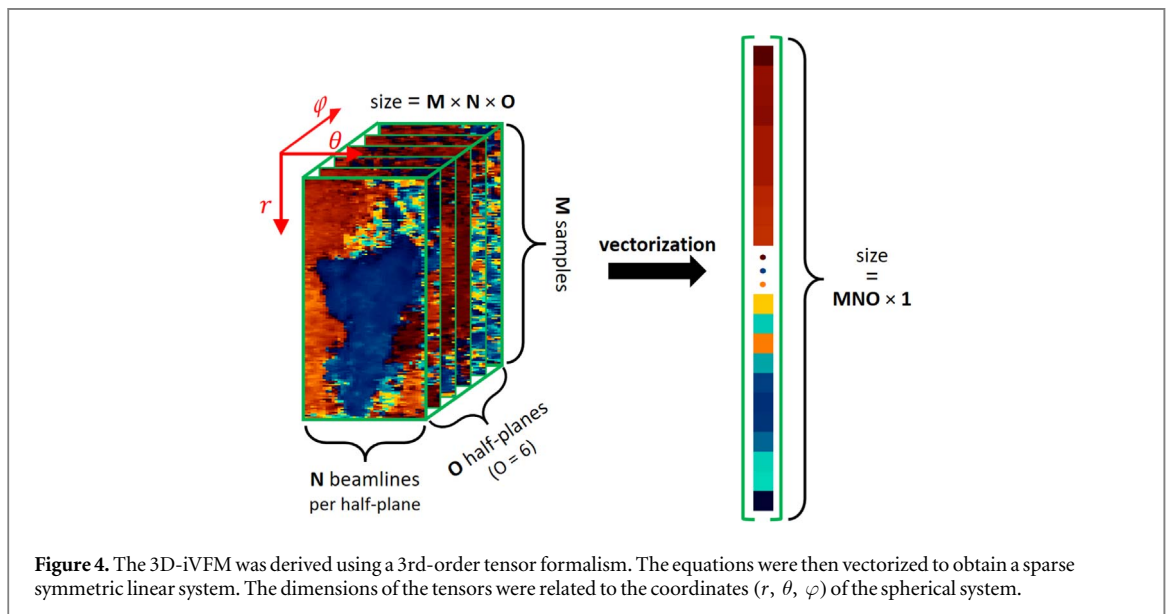### 2.2. iVFM as a constrained minimization problem

The 3D-*i*VFM method starts with the three color Doppler planes given by the triplane mode (figure 2). Because they are not scan-converted, we can write the problem in a spherical coordinate system (figure 3). In this coordinate system, the Doppler velocities (u_{D}) are estimates of the radial velocities (v_r) (with an opposite sign, the Doppler velocities being positive towards the probe) corrupted by noise (η):

$$v_r(r, \theta, \varphi) = -u_{\mathrm{D}}(r, \theta, \varphi) + \eta(r, \theta, \varphi). \tag{1}$$

The objective of 3D-*i*VFM is to deduce the radial, polar, and azimuthal velocity components $[v_r(r, \theta, \varphi), v_\theta(r, \theta, \varphi), \text{and } v_\varphi(r, \theta, \varphi)]$ in the full left ventricular volume, from the Doppler velocities (u_{D}) of the three planes. In the following, we briefly describe the minimization problem and its numerical solution. To facilitate the derivation of the linear system, the six Doppler half-planes were stacked to build a 3rd order tensor (figure 4), with each dimension corresponding to a spherical coordinate. The equations of the numerical scheme were then vectorized (figure 4) to form a standard matrix-vector linear system.

Figure 2. In the 3D-*i*VFM (intraventricular Vector Flow Mapping) technique, we use the Doppler velocities (1st row) and endocardial displacements (from the B-mode images, 2nd row) before scan-conversion, i.e. in the coordinate system defined in figure 3. The 3rd row is the corresponding triplane view.

We extended the 2D-*i*VFM algorithm proposed by Assi *et al* (2017) and added physics-based equality constraints to obtain a hemodynamically valid estimate (Vixège *et al* 2021b). The hemodynamic equality constraints, based on fluid dynamics, ensured that the reconstructed flow was divergence-free (mass conservation for an incompressible fluid) and slipped freely on the endocardial wall (free-slip boundary conditions). We wrote the optimization problem as a constrained regularized least-squares problem, which was solved using the Lagrange multiplier method (Kalman 2009). It was mathematically written as follows:

Figure 3. The data and equations that are included in 3D-iVFM (intraventricular Vector Flow Mapping) are expressed in this spherical coordinate system.

Figure 4. The 3D-iVFM was derived using a 3rd-order tensor formalism. The equations were then vectorized to obtain a sparse symmetric linear system. The dimensions of the tensors were related to the coordinates (r, θ, φ) of the spherical system.

$$\vec{v}_{\text{VFM}} = \underset{\vec{v}}{\arg\min} \, J(\vec{v}). \tag{2}$$

From (1), the cost function was written as

$$J(\vec{v}) = \int_{\Omega} (v_r + u_D)^2 \mathrm{d}\Omega + \alpha \mathcal{L}(\vec{v}). \tag{3}$$

The cost function J was minimized subject to the following equality constraints:

$$\begin{cases} \operatorname{div}(\vec{v}) = 0 & \text{on } \Omega, \\ \vec{v} \cdot \vec{n}|_{\text{wall}} - \vec{v}_{\text{wall}} \cdot \vec{n}|_{\text{wall}} = 0 & \text{on } \partial\Omega. \end{cases} \tag{4}$$

$\vec{v}_{\text{VFM}}$ are the estimated three-component velocity vectors. The function $\mathcal{L}(\vec{v})$ induces spatial smoothing. It contains second-order partial derivatives of the velocity, with cross-terms, with respect to the radial and polar coordinates (r, θ). We used the same smoothing function as in Assi *et al* (2017). The parameter α is the regularization smoothing parameter (a scalar), which was determined by using the L-curve method (see section '*Selection of the Smoothing Parameter*'). Ω stands for the intracavitary region of interest, and $\partial\Omega$ is its boundary (endocardium). $\vec{n}|_{\text{wall}}$ is the unit vector normal to the endocardial wall, and $\vec{v}_{\text{wall}}$ is the endocardial wall velocity.

The first equality constraint in (4) ensures mass conservation. By expressing the divergence in spherical coordinates then multiplying by $r \sin(\theta)$, it can be rewritten as

$$
\begin{aligned}
&\mathrm{div}(\vec{v}) = 0 \Rightarrow \\
&2 \sin(\theta) v_r + r \sin(\theta) \partial_r v_r + \cos(\theta) v_\theta \\
&+ \sin(\theta) \partial_\theta v_\theta + \partial_\varphi v_\varphi = 0 \ \ \text{on } \Omega.
\end{aligned}
\tag{5}
$$

The second equality imposes free-slip boundary conditions. Because we work with 2D images (planes), the azimuthal component of $\vec{v}_{\mathrm{wall}}$ ($v_{wall\ \varphi}$) is not available. To ensure well-posedness of the 3D-*i*VFM problem, we assumed that $v_\varphi = 0$ on $\partial\Omega$. The boundary conditions [second constraint in equation (4)] were thus rewritten as:

$$
\begin{aligned}
&(v_r - v_{wall\ r})\, n_{wall\ r} + (v_\theta - v_{wall\ \theta})\, n_{wall\ \theta} = 0, \\
&\text{and } v_\varphi = 0 \ \ \text{on } \partial\Omega.
\end{aligned}
\tag{6}
$$

The spherical 3D grid used for 3D-*i*VFM has constant radial, polar, and azimuthal steps (h_r, h_θ, and h_φ). We used a finite-difference discretization scheme (with second-order central differences) to convert this constrained least-squares problem into a matrix-vector form. The Doppler velocities were stored in a 3rd-order tensor of size ($M \times N \times O$), where M is the number of samples per scanline, N is the number of scanlines per half-plane, and O is the number of half-planes (i.e. $O = 6$ for a triplane mode, figure 4). The numerical counterpart of the constrained least-squares problem described by equations (2)–(6) was written using a tensor formalism, then vectorized (figure 4), to obtain a sparse symmetric linear system. We briefly describe the linear system in the following.

The vectorization led to column vectors. We note these column vectors as follows:

- $\boldsymbol{u_D}$, of length (MNO), contains the Doppler velocities.

- $\boldsymbol{r}$, $\boldsymbol{\theta}$, $\boldsymbol{\varphi}$, of length (MNO), contain the radial, polar, and azimuthal coordinates, respectively.

- $\boldsymbol{n_r}$ and $\boldsymbol{n_\theta}$, of length (MNO), contain the radial and polar coordinates of the unit vector normal to the cardiac inner wall (endocardium). They are zero if the node does not belong to the endocardium.

- $\boldsymbol{\delta}$, of length (MNO), is a binary vector that represents the intracavitary region of interest (ROI). It is 1 if the node is inside or on the edge of the left ventricular cavity, 0 otherwise.

- $\partial\boldsymbol{\delta}$, of length ($MNO$), is a binary vector that represents the endocardial wall. It is 1 if the node is on the endocardium, 0 otherwise.

- $\boldsymbol{v} = [\boldsymbol{v_r}^\mathrm{T}\ \boldsymbol{v_\theta}^\mathrm{T}\ \boldsymbol{v_\varphi}^\mathrm{T}]^\mathrm{T}$, of length ($3\,MNO$), is a column vector that contains the *i*VFM solution of the minimization problem.

- $\boldsymbol{v}_{\mathrm{wall}} = [\boldsymbol{v}_{\mathrm{wall},\boldsymbol{r}}^\mathrm{T}\ \boldsymbol{v}_{\mathrm{wall},\boldsymbol{\theta}}^\mathrm{T}\ \boldsymbol{v}_{\mathrm{wall},\boldsymbol{\varphi}}^\mathrm{T}]^\mathrm{T}$, with $\boldsymbol{v}_{\mathrm{wall},\boldsymbol{\varphi}} = 0$ everywhere [see equation (6)], of length ($3\,MNO$), is a column vector that contains the radial, polar and azimuthal (=0) components of the endocardial velocities. They are zero if the node does not belong to the endocardium.

- $\boldsymbol{\lambda}_1$ and $\boldsymbol{\lambda}_2$, of respective lengths (MNO) and ($2\,MNO$), contain the Lagrangian multipliers associated with the 1st (divergence-free) and 2nd (boundary) equality constraints.

The *i*VFM minimization problem contains the Q_0, Q_1, Q_2, and $Q_\mathcal{L}$ matrices that are introduced in the next paragraph. The matrix Q_0 is related to the fitting to Doppler velocities (3). Q_1 and Q_2 are related to the 1st (5) and 2nd equality constraints (6). $Q_\mathcal{L}$ is associated with the smoothing regularizer included in (3). We also define the following matrices and vectors:

- $\dot{D}_q$ and $\ddot{D}_q$, both of size ($q \times q$), are finite-difference matrices for the 1st and 2nd derivatives, respectively.

- $\mathbb{O}_q$ and $\mathbb{I}_q$, both of size ($q \times q$), are the zero and identity matrices, respectively.

- 0_q is a vector of zeros of size ($q \times 1$).

In the following, $\otimes$ and $\circ$ stand for the Kronecker and Hadamard (element-wise) products. A least-squares numerical solution of the minimization problem given by (2) and (3), subject to the equality constraints (5) and (6), can be determined through the Lagrange multiplier method (Kalman 2009). It is given by seeking the vectors $\boldsymbol{v}$, $\boldsymbol{\lambda}_1$, and $\boldsymbol{\lambda}_2$ that minimize

$$J_L(\boldsymbol{v}, \boldsymbol{\lambda}_1, \boldsymbol{\lambda}_2) = (Q_0\boldsymbol{v} + \boldsymbol{u_D})^{\mathrm{T}}(Q_0\boldsymbol{v} + \boldsymbol{u_D})$$
$$+\alpha(Q_{\mathcal{L}}\boldsymbol{v})^{\mathrm{T}}(Q_{\mathcal{L}}\boldsymbol{v}) + \boldsymbol{\lambda}_1^{\mathrm{T}}Q_1\boldsymbol{v} + \boldsymbol{\lambda}_2^{\mathrm{T}}Q_2\boldsymbol{v}. \tag{7}$$

The Q-matrices are given by (supplementary document (available online at stacks.iop.org/PMB/67/095004/mmedia)):

$$Q_0 = [1\ 0\ 0] \otimes \mathrm{diag}(\boldsymbol{\delta})$$

$$Q_1 = \Bigg[\ 2\,\mathrm{diag}(\sin(\boldsymbol{\theta})\circ\boldsymbol{\delta}) + \frac{1}{h_r}\mathrm{diag}(\boldsymbol{r}\circ\sin(\boldsymbol{\theta})\circ\boldsymbol{\delta})\,(\mathbb{I}_O \otimes \mathbb{I}_N \otimes \dot{D}_M),$$

$$\mathrm{diag}(\cos(\boldsymbol{\theta})\circ\boldsymbol{\delta}) + \frac{1}{h_\theta}\mathrm{diag}(\sin(\boldsymbol{\theta})\circ\boldsymbol{\delta})\,(\mathbb{I}_O \otimes \dot{D}_N \otimes \mathbb{I}_M),$$

$$\frac{1}{h_\varphi}\mathrm{diag}(\boldsymbol{\delta})\,(\dot{D}_O \otimes \mathbb{I}_N \otimes \mathbb{I}_M)\Bigg]$$

$$Q_2 = \begin{bmatrix} \mathrm{diag}(\boldsymbol{n_r}), & \mathrm{diag}(\boldsymbol{n_\theta}), & \mathbb{O}_{MNO} \\ \mathbb{O}_{MNO}, & \mathbb{O}_{MNO}, & \mathrm{diag}(\partial\boldsymbol{\delta}) \end{bmatrix}$$

$$Q_{\mathcal{L}} = \begin{bmatrix} \mathbb{I}_3 \otimes \left(\dfrac{1}{h_r{}^2}\mathrm{diag}(\boldsymbol{r}\circ\boldsymbol{r}\circ\boldsymbol{\delta})\,(\mathbb{I}_O \otimes \mathbb{I}_N \otimes \ddot{D}_M)\right) \\[2ex] \mathbb{I}_3 \otimes \left(\dfrac{1}{h_\theta{}^2}\mathrm{diag}(\boldsymbol{\delta})\,(\mathbb{I}_O \otimes \ddot{D}_N \otimes \mathbb{I}_M)\right) \\[2ex] \mathbb{I}_3 \otimes \left(\dfrac{\sqrt{2}}{h_r h_\theta}\mathrm{diag}(\boldsymbol{r}\circ\boldsymbol{\delta})\,(\mathbb{I} \otimes \dot{D}_N \otimes \dot{D}_M)\right) \end{bmatrix}. \tag{8}$$

The Q_0, Q_1, Q_2, and $Q_{\mathcal{L}}$ matrices are of size ($MNO \times 3MNO$), ($MNO \times 3MNO$), ($2MNO \times 3MNO$), and ($9MNO \times 3MNO$), respectively. The Kronecker products between the identity and D matrices are related to the 1st- and 2nd-order derivatives. Minimizing $J_L(\boldsymbol{v}, \boldsymbol{\lambda}_1, \boldsymbol{\lambda}_2)$ yields the linear system

$$A\boldsymbol{x} = \boldsymbol{b}, \text{ with}$$

$$A = \begin{bmatrix} 2(Q_0{}^T Q_0 + \alpha Q_{\mathcal{L}}{}^T Q_{\mathcal{L}}) & Q_1{}^T & Q_2{}^T \\ Q_1 & & \\ Q_2 & & \mathbb{O}_{3MNO} \end{bmatrix}$$

$$\boldsymbol{x} = \begin{bmatrix} \boldsymbol{v} \\ \boldsymbol{\lambda}_1 \\ \boldsymbol{\lambda}_2 \end{bmatrix}, \qquad b = \begin{bmatrix} -2Q_0\boldsymbol{u_D} \\ 0_{MNO} \\ Q_2\boldsymbol{v}_{\mathrm{wall}} \end{bmatrix}. \tag{9}$$

The matrix A is sparse symmetric and of size ($6MNO \times 6MNO$). $\boldsymbol{b}$ and $\boldsymbol{x}$ are column vectors of size ($6MNO \times 1$). The linear system (9) illustrates the basic principles of 3D-iVFM. Rather than solving directly this system, we have completed it by parameterizing the velocity field as now explained.

2.3. Parametrization of the velocity field

The 3D-iVFM velocimetric method uses a clinical triplane mode, which provides three long-axis planes (i.e. six azimuthal half-planes, figures 2 and 4). Although Doppler sampling is appropriate in the radial and polar directions, it is limited in the azimuthal direction (6 samples). To obtain proper azimuthal derivatives and ensure a full-volume reconstruction, we expressed the velocity components by a parametrized function that is periodic in the azimuthal direction:

$$v_k = c0_k(r, \theta) + c1_k(r, \theta)\cos(\varphi) + c2_k(r, \theta)\cos(2\varphi)$$
$$+c3_k(r, \theta)\cos(3\varphi) + c4_k(r, \theta)\sin(\varphi) + c5_k(r, \theta)\sin(2\varphi),$$
$$\text{with } k \in \{r\theta\varphi\}. \tag{10}$$

The parametrized v_k contained six parameters since we had six half-planes. These coefficients (cP_r, cP_θ, and cP_φ, with $P = 0 \ldots 5$) were stored in a column vector $\boldsymbol{c}$ of length ($18MN$) (3 coordinates $\times$ 6 half-planes $\times$ MN samples per half-plane). The linear system (9) was modified to include the coefficients of the parametrized velocities: all Q matrices were multiplied by sparse matrices containing the coefficients $\{1, \cos(\varphi), \cos(2\varphi), \ldots\}$ of the expression (10). After parametrization of the velocity field, the linear system (9) became

Figure 5. Automatic selection of the regularization scalar: an L-curve is plotted from a set of regularization parameters (black dots). We choose the regularization parameter that provides the rising point of inflection (here $10^{-5.5}$, red dot). This example is from a patient at the end of early filling. In practice, we used five α values to generate an L-curve by fitting an hyperbolic tangent function.

$$A\boldsymbol{x} = \boldsymbol{b}, \ \text{with } \boldsymbol{x} = \begin{bmatrix} \boldsymbol{c} \\ \lambda_1 \\ \lambda_2 \end{bmatrix}. \tag{11}$$

The A matrix, and the $\boldsymbol{x}$ and $\boldsymbol{b}$ vectors, obtained after parametrization, are described in the supplementary document. Solving the system (11) yields the coefficients $\boldsymbol{c}$ and, in turn, the full-volume three-component velocity fields. The A matrix is rank-deficient because it contains columns and rows of zeros, as the region of interest and its boundary do not cover the entire domain. After having discarded the null rows and columns to make the matrix full-rank and positive-definite, we solved the sparse linear system (11) in MATLAB (MathWorks) by using an LDL decomposition.

2.4. Selection of the smoothing parameter

The linear system (11) contains a regularization scalar (α) that adjusts the effect of smoothing given by the $Q_{\mathcal{L}}$ matrix. To make the iVFM technique unsupervised, we selected the smoothing parameter automatically through the L-curve method (Hansen 2000). This method helps in identifying the trade-off between the amount of regularization (smoothing) and the quality of the fit to the input (Doppler) data. The L-curve consists of a log-log plot of the residual norm versus the regularization norm for a set of α values. In our case, the 'optimal' α was the one that corresponded to the rising point of inflection of the L-curve. Figure 5 depicts an L-curve obtained in one volunteer (see also figure 10). To obtain the L-curve, we decomposed the matrix A into two parts: a constrained data-fitting matrix A_1, and a matrix A_2 related to the smoothing, which reads as follows:

$$A = A_1 + \alpha A_2, \ \text{where}$$

$$A_1 = \begin{bmatrix} 2Q_0^T Q_0 & Q_1^T & Q_2^T \\ Q_1 & & \\ Q_2 & & \mathbb{O}_{3MNO} \end{bmatrix}$$

$$A_2 = \begin{bmatrix} 2Q_{\mathcal{L}}^T Q_{\mathcal{L}} & \mathbb{O}_{3MNO} \\ \mathbb{O}_{3MNO} & \mathbb{O}_{3MNO} \end{bmatrix}. \tag{12}$$

From these matrices, the L-curve associated with the linear system (11) was given by

$$\{\log(\|A_1 \, x(\alpha) - \boldsymbol{b}\|_2), \ \log(\|A_2 \, x(\alpha)\|_2)\}. \tag{13}$$

The L-curve method requires solving the linear system with several values of α. We used several α parameters to generate an L-curve and determine its 'optimal' α_{opt} value. To reduce computational time, it is preferred not to repeat this process for each triplane color-Doppler. Therefore, we calculated the L-curve, and its corresponding optimal α_{opt}, once, at the end of early filling. We then used this same α_{opt} value for the whole cardiac cycle.

2.5. *In silico* validation

Validating the 3D-*i*VFM algorithm required full-volume three-component ground-truth velocity fields of the intraventricular blood flow. We used a patient-specific CFD (computational fluid dynamics) model (Chnafa *et al* 2014, 2016), as for the latest versions of 2D-*i*VFM (Assi *et al* 2017, Vixège *et al* 2021b). We interpolated the radial components (figure 3) of the CFD velocity vectors onto three planes (as in figure 2) to simulate triplane color Doppler. One hundred triplane echocardiographic scans were simulated for one cardiac cycle. The radial and polar steps were 0.55 mm and 0.45°. Each half-plane contained 8000 Doppler-velocity samples ($M = 160$, and $N = 50$). Gaussian white noise with velocity-dependent local variance (signal-to-noise ratio ranging between 20 and 50 dB with a 10 dB step) was added, as in Muth *et al* (2011). Based on these simulated triplane Doppler velocities, the coefficients of the parametrized *i*VFM velocities, given by (10), were calculated by solving the linear system (11). From these coefficients, we generated full-volume three-component intraventricular velocity fields on an $M \times N \times 24$ spherical grid (i.e. on 24 half-planes). We compared the *i*VFM-derived velocity components against the actual CFD-based velocity components by regression analysis and by calculating the normalized root-mean-square errors (nRMSE) for each noise level:

$$\text{nRMSE} = \frac{1}{\max(\|\vec{v}_{\text{CFD}}\|)} \sqrt{\frac{1}{LVV} \int \|\boldsymbol{v}_{k-\text{CFD}} - \boldsymbol{v}_{k-\text{iVFM}}\|^2 \; r^2 \sin(\theta) \; \mathrm{d}r \mathrm{d}\theta \mathrm{d}\varphi}$$
$$\text{with } k \in \{r, \; \theta, \; \varphi\}. \tag{14}$$

In equation (14), LVV stands for the left ventricular volume. In addition, we computed the radial, polar, and azimuthal components of the vorticity, as well as its amplitude, for both CFD and *i*VFM, and we compared their means. We finally estimated the vortex volumes by using the Q-criterion (Günther and Theisel 2018): a voxel belonged to a vortex if its Q-value was greater than a predefined threshold. The threshold was ranged between 5000 and 15 000 s^{-2} to get several volume estimates per time step. We compared the mean vortex volumes (CFD versus *i*VFM) over diastole. The vorticities (ω), Q-criterion, and vortex volumes of the CFD flow data were calculated using ParaView (Kitware Inc., NY, USA), an open-source package for data analysis and visualization. Those derived by *i*VFM were estimated through in-house MATLAB codes.

2.6. *In vivo* analysis

We tested the clinical feasibility of 3D-*i*VFM prospectively, during a routine echocardiographic examination, in one healthy volunteer and in three patients selected on the basis of image quality. The patients had different heart diseases: transthyretin amyloid cardiomyopathy, hypertrophic obstructive cardiomyopathy, and paroxysmal atrial fibrillation. Triplane echocardiography is part of the standard examination protocol. The retrospective study of anonymized data was approved by the local ethics committee. The cardiologist acquired the two-, three-, and four-chamber apical long-axis views using a triplane color Doppler mode with a GE Vivid E95 scanner (figure 1). We selected triplane echocardiographic data that provided good-quality B-mode and Doppler images (echogenic patients, complete left ventricle in all three planes, no visible artifacts). We obtained ~11 color-Doppler triplanes per cardiac cycle. The Doppler velocities and B-mode images (before scan-conversion, figure 2) were saved in Hierarchical Data Format with the EchoPAC clinical software package (GE Healthcare) then post-processed using MATLAB programming. We delineated the endocardial walls manually by using an in-house MATLAB application. The wall velocities were estimated from the endocardial displacements between two successive frames. We finally computed the full-volume three-component intraventricular velocity fields with the 3D-*i*VFM method. Creating the sparse matrices and solving the linear system required ~20 s with a MATLAB code running on the CPU. The vortical regions were detected by using the Q-criterion, and the intraventricular blood flows were visualized through streamlines.

3. Results

3.1. *In silico* results

As illustrated by figures 6, 3D-iVFM enabled the reconstruction of full-volume three-component intraventricular velocity fields from three color-Doppler long-axis planes (triplane color Doppler). In particular, the vortex rings that formed during left ventricular filling (frame #50), and the large rotating circulation at the end of filling (frame #60) were recovered. The *i*VFM-derived flow structures were consistent with those of the CFD ground-truth. The mean velocity errors were the smallest for the radial r-components (less than 3%), while the mean errors on the azimuthal φ-components ranged between 5% and 15% (figure 7). The regression analyses confirmed these results. The 3D-*i*VFM technique reconstructed the radial components with accuracy ($r = 0.99$) since the input information from color Doppler is essentially radial. The regression coefficients obtained with the polar and azimuthal components were $r = 0.78$ and $r = 0.57$, respectively. This trend is also apparent in the error maps. Figure 8 shows the frames (50, 55, and 60) corresponding to the instant of the cardiac
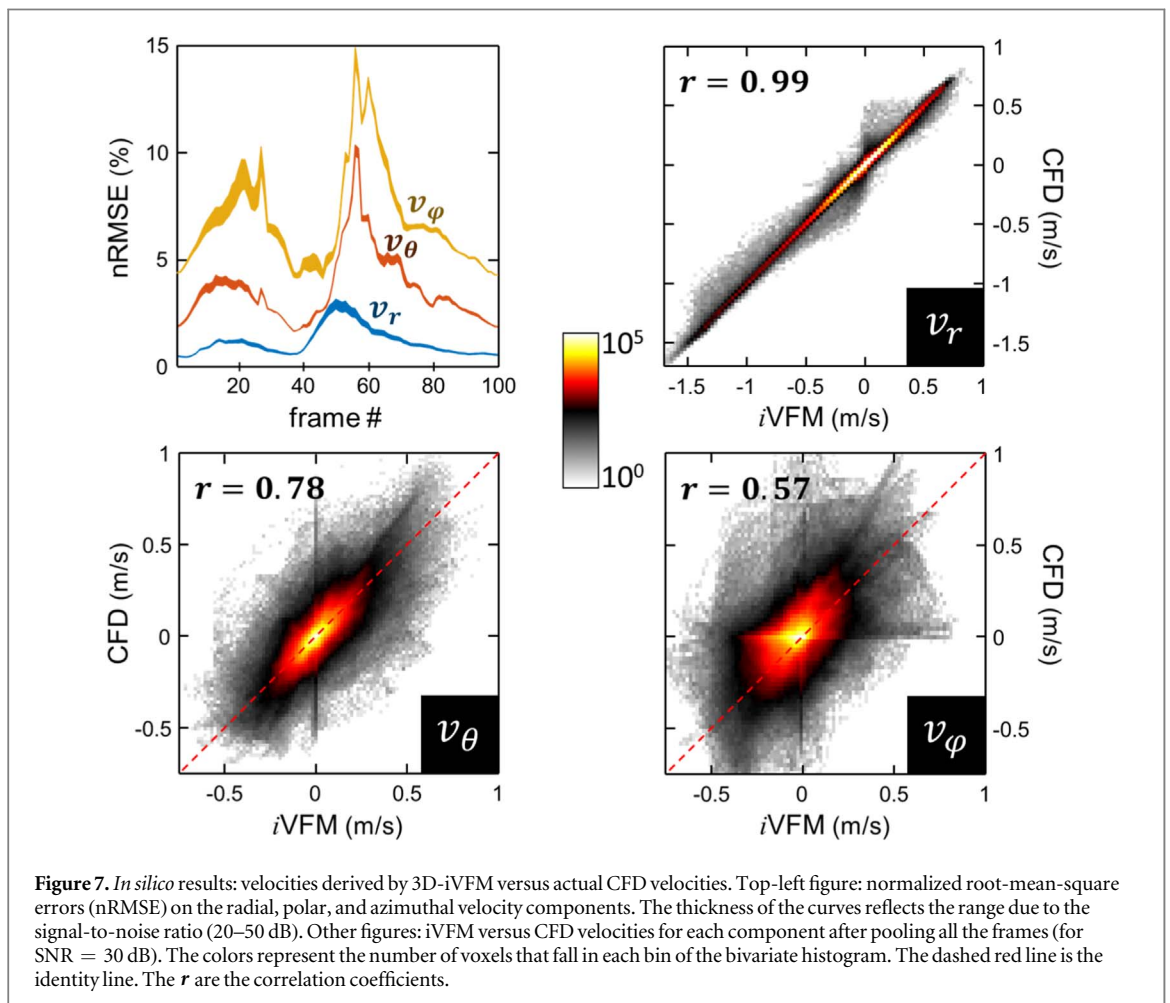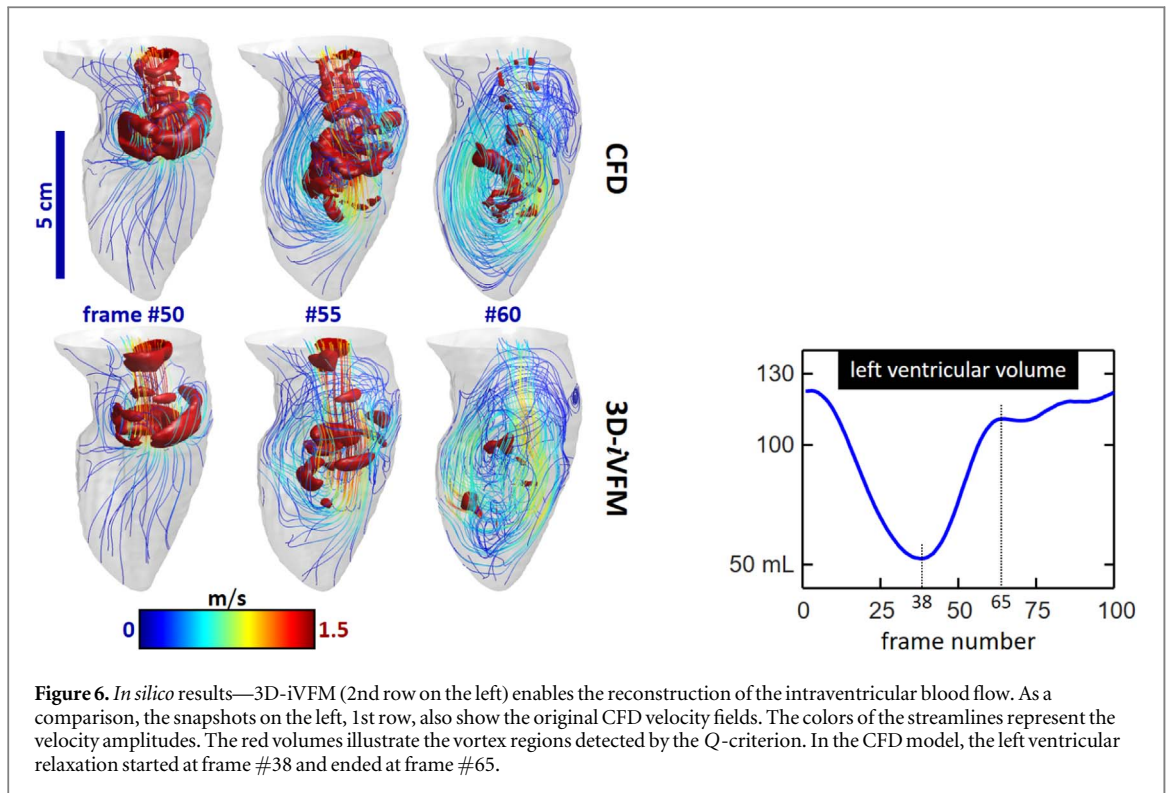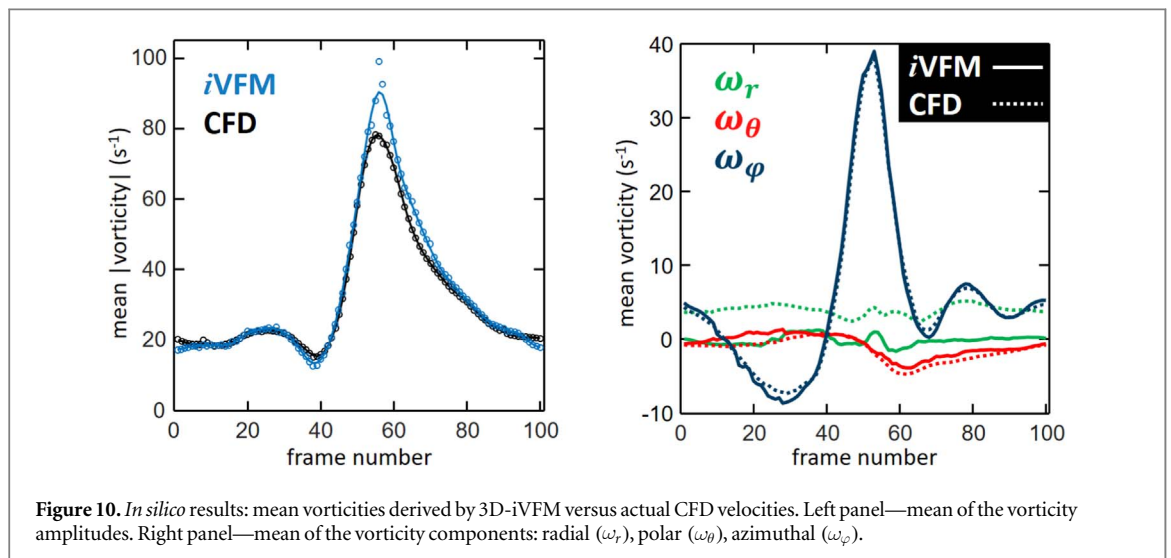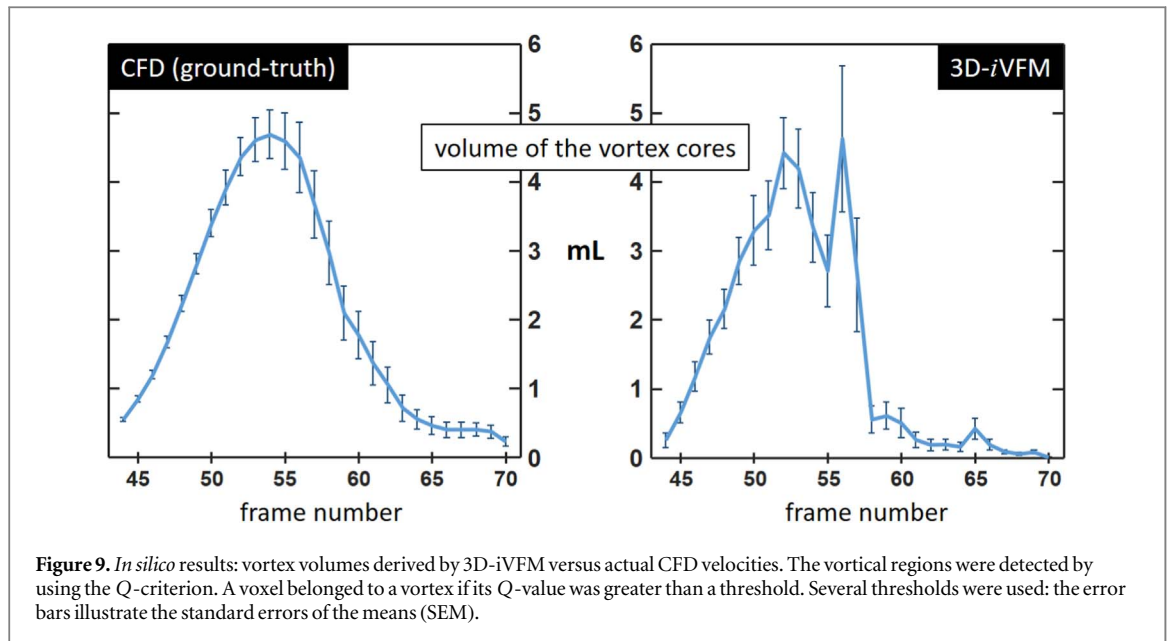
Figure 6. *In silico* results—3D-iVFM (2nd row on the left) enables the reconstruction of the intraventricular blood flow. As a comparison, the snapshots on the left, 1st row, also show the original CFD velocity fields. The colors of the streamlines represent the velocity amplitudes. The red volumes illustrate the vortex regions detected by the Q-criterion. In the CFD model, the left ventricular relaxation started at frame #38 and ended at frame #65.

Figure 7. *In silico* results: velocities derived by 3D-iVFM versus actual CFD velocities. Top-left figure: normalized root-mean-square errors (nRMSE) on the radial, polar, and azimuthal velocity components. The thickness of the curves reflects the range due to the signal-to-noise ratio (20–50 dB). Other figures: iVFM versus CFD velocities for each component after pooling all the frames (for SNR = 30 dB). The colors represent the number of voxels that fall in each bin of the bivariate histogram. The dashed red line is the identity line. The r are the correlation coefficients.

Figure 8. *In silico* results: maps of the normalized errors. The rows refer to the radial, polar, and azimuthal velocity components, respectively. The columns refer to the three planes similar to those of the triplane mode. The frames #50, #55, and #60, occurred during early filling (see figure 6).

cycle when the errors were greatest. Although the large errors on the radial components were mostly confined around the mitral leaflets, those for the polar and azimuthal components followed the vortex ring and spread throughout the left ventricle. The errors on the radial, polar, and azimuthal components reflect the voxelwise (local) biases in velocity estimation. The goal of 3D-*i*VFM, however, is to deduce global biomarkers that describes the intraventricular flow. Figures 9 and 10 show how global vorticity parameters evolved. The volumes of the vortex cores (figure 9), as determined by the Q-criterion (red volumes in figure 6), were the largest at mid-filling (around frame #55). The vortex volumes derived from *i*VFM agreed with those measured in the CFD model but contained some inconsistencies (figure 9). The peak of the mean vorticity amplitude was reached (80–90 s^{-1}) around frame #55 (figures 6, and 10, left). The azimuthal vorticity components (ω_φ) were the most
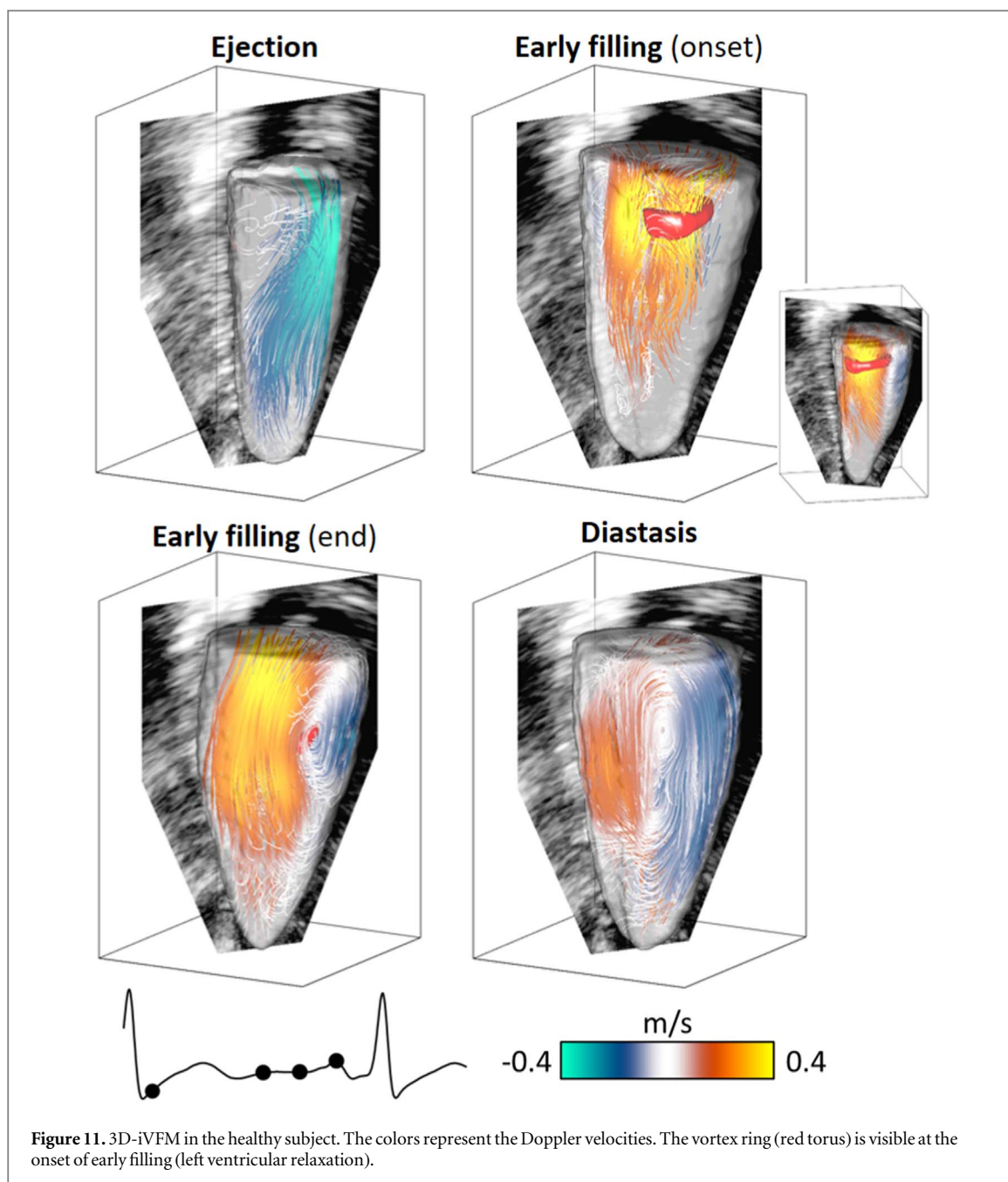
Figure 9. *In silico* results: vortex volumes derived by 3D-iVFM versus actual CFD velocities. The vortical regions were detected by using the Q-criterion. A voxel belonged to a vortex if its Q-value was greater than a threshold. Several thresholds were used: the error bars illustrate the standard errors of the means (SEM).

Figure 10. *In silico* results: mean vorticities derived by 3D-iVFM versus actual CFD velocities. Left panel—mean of the vorticity amplitudes. Right panel—mean of the vorticity components: radial (ω_r), polar (ω_θ), azimuthal (ω_φ).

prominent (figure 10, right) compared with the radial (ω_r) and polar (ω_θ) components. 3D-*i*VFM produced vorticity profiles consistent with those given by CFD (ground-truth).

3.2. Feasibility of 3D-iVFM in patients

The 3D-*i*VFM technique enabled the reconstruction of intraventricular flows in selected patients after a routine echocardiographic examination. Figure 11 displays the flow streamlines in the healthy subject at different stages of the cardiac cycle. The vortex ring formed by the mitral jet at the onset of early filling (i.e. ventricular relaxation) is visible. A large long-axis circular motion then occupies the entire intraventricular cavity at the end of early filling and during diastasis (the period between ventricular relaxation and atrial contraction). Figure 12 displays diastolic flow streamlines in three patients with heart disease.

In this work, we do not provide comparative measurements using 4D flow MRI. Nevertheless, it can be appreciated that the flows we reconstructed have strong qualitative similarities with intracardiac flows measured by others with MRI. For illustrative purposes, we invite the reader to refer to figure 1 of Eriksson *et al* (2010), and figure 2 of Eriksson *et al* (2013). The vortex rings visible in figures 11 and 12 are also consistent with those reported in other studies that have involved MRI, as seen in figure 7 of Markl *et al* (2011) and figure 3 of Faurie *et al* (2017).
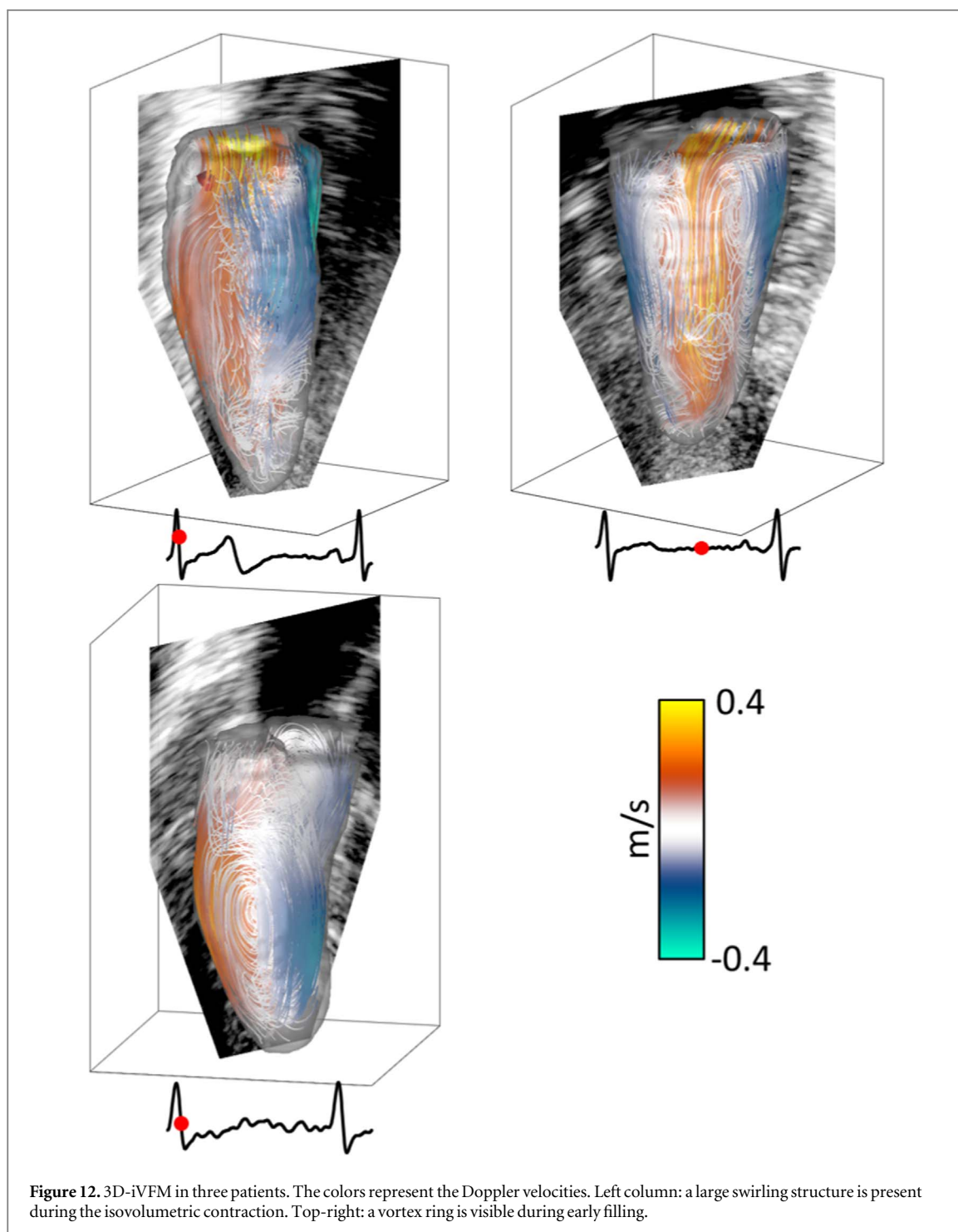
Figure 11. 3D-*i*VFM in the healthy subject. The colors represent the Doppler velocities. The vortex ring (red torus) is visible at the onset of early filling (left ventricular relaxation).

4. Discussion

4.1. Quality of the reconstructed vector field

The 3D-*i*VFM introduced in this article allows the reconstruction of full-volume three-component intraventricular flows from triplane color Doppler. This mode provides three long-axis apical views separated by an azimuthal angle of sixty degrees. In the spherical coordinate system associated with the cardiac probe, the triplane mode measures the radial components of the velocities, with noise. The 3D-*i*VFM problem has essentially two unknowns, which are the polar and azimuthal angular components of the velocities. For comparison, only the polar components are sought with the 2D-*i*VFM that operates in a three-chamber view. As we did for the 2D-*i*VFM, the 3D-*i*VFM was validated using an intracardiac CFD model. This CFD model has the advantage of providing realistic reference intraventricular flows at high spatial and temporal resolutions.

As expected, the radial components of the velocity field were the best reconstructed, with errors less than 3%. The differences, mostly visible around the mitral leaflets, originated from the smoothing and inter-angle interpolation imposed by the *i*VFM method. The errors on the polar components were close to those observed with the recent version of the 2D-*i*VFM (Vixège *et al* 2021b), ranging between 2% and 10%. On the other hand, the azimuthal components were the most error-prone because we had little information in this direction. Only

Figure 12. 3D-iVFM in three patients. The colors represent the Doppler velocities. Left column: a large swirling structure is present during the isovolumetric contraction. Top-right: a vortex ring is visible during early filling.

six samples (six half-planes) were available. To compensate for this azimuthal undersampling, we used a parametric periodic formulation of the velocities, given by equation (10). The errors in velocities were greatest at the beginning of ventricular filling. This is a phase in the flow where polar and azimuthal velocities become significant. The vortex changes from a ring to a recirculation shape. Despite significant azimuthal errors, the global aspect of the flow was adequately recovered (figure 9). More importantly, the global vorticity was determined accurately, which tends to show that the 3D-*i*VFM could be used for physiological purposes to characterize the intracavitary left ventricular flows.

4.2. Technical and numerical limitations

Intracardiac blood flow is three-dimensional and changes rapidly during a cardiac cycle. A conventional triplane color Doppler returns around 10 triplane sequences per second. To obtain a triplane sequence, a series of focused or narrow ultrasound beams are transmitted sequentially in the radial direction to scan the planes of

interest. The spatial resolution of one plane is approximately 0.6 mm by 1.4 degrees. In addition, for each radial direction, about six ultrasound beams are transmitted to enable Doppler velocities to be determined. It results that there is a significant time delay between the first Doppler line of the first plane and the last Doppler line of the third plane. A triplane dataset, therefore, has a limited spatiotemporal resolution. Given the limitations of triplane color Doppler, 3D-*i*VFM can only provide smoothed estimates of the velocity fields. Although several researchers have reported measuring energy dissipation due to blood viscosity in turbulent flow by two-dimensional *i*VFM (Stugaard *et al* 2015, Zhong *et al* 2016), this claim is incorrect. The fluctuating quantities of turbulent flow cannot be captured by color Doppler. Nevertheless, the results obtained with the CFD model show that it would be possible to measure global vortical indices (figure 9). In particular, we anticipate that the peak of global vorticity could reflect the filling function. This remains to be demonstrated, as our study does not allow such a conclusion. We qualitatively tested the algorithmic methodology and evaluated its feasibility in a clinical setting. For this purpose, we generated noisy 'ideal' Doppler fields from the radial velocity components given by the CFD model. Our results thus do not allow us to conclude on the effects of ultrasound imaging artifacts, such as clutters related to wall motions and sidelobes or grating lobes, and dropouts due to clutter filtering. A study coupling fluid dynamics and acoustics would complete the validations and provide insights into these issues. An approach would be the use of ultrasound simulations (Cigier *et al* 2021, Garcia 2021) after seeding the CFD flow with scattering particles (Swillens *et al* 2010, Shahriari and Garcia 2018).

4.3. From 2D, to 3D, to 4D?
The *i*VFM that we introduced in this work is a three-dimensional upgrade of the previous 2D version (Vixège *et al* 2021b). We could even claim that it is a 4D version (volume + time) because temporal information is also available. The temporal resolution ($\sim$10 volumes s^{-1}) is nevertheless limited by that of triplane color Doppler. The rate of *i*VFM volumes is similar to that of 4D MRI velocimetry. Under the condition that the heart rate is sufficiently stable, it would then be necessary to analyze more than five cardiac cycles to decipher the flow dynamics with sufficient accuracy. This is precisely the approach used in 4D flow CMR, with respiratory navigator gating. The temporal limitation of triplane echocardiography is related to the sectorial line-by-line scanning of each of the three planes. A promising solution would be the use of diverging rather than focused waves (Faurie *et al* 2017, 2019). Such an alternative of high-frame-rate triplane echocardiography, with simulated spiral arrays, has been proposed by Ramalli *et al* using multi-line transmits and diverging waves (Ramalli *et al* 2020). Another approach would be the use of high-volume-rate color Doppler (Provost *et al* 2014), which would have the twofold advantage of increasing temporal resolution and providing more Doppler information (full volumes instead of three planes).

4.4. What still needs to be done
We showed that three-dimensional reconstruction of intracardiac flow is feasible during a routine clinical examination. We used triplane echocardiography and Doppler data before scan-conversion through GE Healthcare EchoPAC clinical software. The time for ultrasound acquisition (<20 s) and 3D velocity calculation (<20 s per volume), was well below that of 4D flow CMR, even though we used a homemade MATLAB code. In this study, we established that 3D-*i*VFM is feasible in patients. Although the *in silico* results were promising, we need to further demonstrate that vector flows estimated in patients are consistent with those provided by phase-contrast CMR. If future studies confirm this agreement, it should also be verified that a vortex-based volume biomarker (e.g. peak vorticity, see figure 9) might be clinically relevant for assessing diastolic function. At the very least, echocardiographic velocimetry by 3D-*i*VFM could be used for physiological purposes to better comprehend the dynamic relationship between the myocardium and intracardiac flow. This goal would be in line with previous works that have made use of high-frame-rate Doppler echocardiography (Faurie *et al* 2019, Papadacci *et al* 2019).

As discussed previously, volumetric Doppler data would likely allow more accurate 3D flow reconstruction, albeit at the expense of temporal resolution. These volume data are generally protected and therefore not accessible for post-processing. Grønli *et al* (in conjunction with GE Healthcare) showed that *i*VFM with volume data is possible (Grønli *et al* 2018). Using TensorFlow, they regularized the velocity fields by imposing mechanical constraints and endocardial boundary conditions. They also succeeded in increasing the volume rate by transmitting wide ultrasound waves. Rather than Doppler velocities, blood speckle tracking has also been proposed for the 2D reconstruction of intracardiac flow (Fadnes *et al* 2014, Nyrnes *et al* 2020, Daae *et al* 2021). It is possible to combine color Doppler with speckle tracking to get the most out of each. This has been achieved for 2D myocardial motion analysis using diverging-wave echocardiography (Porée *et al* 2018). This approach could theoretically be applicable in 3D for intracardiac flows. In addition to beamforming, motion detection, and regularization methods, *i*VFM is also dependent on clutter filtering, dealiasing, and endocardial segmentation. Having made use of a clinical ultrasound device, we did not have control over the wall filter. The dealiasing

method that we used was an unwrapping technique introduced by Muth *et al* (2011). It depends on an input variable that sometimes had to be adjusted manually. To make dealiasing fully automatic, we will resort to deep learning (Nahas *et al* 2020). In our study, the endocardial segmentation was performed manually for the analysis of the clinical cases. This step was necessary to determine the boundary conditions. To avoid this time-consuming task, a future version of 3D-*i*VFM will include deep learning-assisted segmentation, as described in Leclerc *et al* (2020). Although there is some room for technical improvements, the 3D-*i*VFM version introduced in our study shows that it is possible to visualize, and quantify, left intraventricular flows in three dimensions. The 3D-*i*VFM could be applicable in a clinical setting since it uses a standard apical echocardiographic window and fast algorithms.

5. Conclusion

We have introduced an updated Doppler-based *i*VFM algorithm for recovering three-component full-volume intraventricular blood flows. For this purpose, we used a minimization problem constrained by equations consistent with fluid dynamics. The model selection was automatized through an *L*-curve to minimize operator dependence. The 3D-*i*VFM is compatible with standard echocardiographic examination and is not time-consuming. Color-Doppler-based 3D-*i*VFM still needs to be compared against 4D-CMR velocimetry in patients.

Acknowledgments

ORCID iDs

Simon Mendez ⓘ https://orcid.org/0000-0002-0863-2024
Damien Garcia ⓘ https://orcid.org/0000-0002-8552-1475

References

Arvidsson P M, Kovács S J, Töger J, Borgquist R, Heiberg E, Carlsson M and Arheden H 2016 Vortex ring behavior provides the epigenetic blueprint for the human heart *Sci. Rep.* **6** 1–9

Assi K C, Gay E, Chnafa C, Mendez S, Nicoud F, Abascal J F P J, Lantelme P, Tournoux F and Garcia D 2017 Intraventricular vector flow mapping-a Doppler-based regularized problem with automatic model selection *Phys. Med. Biol.* **62** 7131–47

Bermejo J, Martínez-Legazpi P and del Álamo J C 2015 The clinical assessment of intraventricular flows *Annu. Rev. Fluid Mech.* **47** 315–42

Charonko J J, Kumar R, Stewart K, Little W C and Vlachos P P 2013 Vortices formed on the mitral valve tips aid normal left ventricular filling *Ann. Biomed. Eng.* **41** 1049–61

Chen P, van Sloun R J G, Turco S, Wijkstra H, Filomena D, Agati L, Houthuizen P and Mischi M 2021 Blood flow patterns estimation in the left ventricle with low-rate 2D and 3D dynamic contrast-enhanced ultrasound *Comput. Methods Prog. Biomed.* **198** 105810

Chnafa C, Mendez S and Nicoud F 2014 Image-based large-eddy simulation in a realistic left heart *Comput. Fluids* **94** 173–87

Chnafa C, Mendez S and Nicoud F 2016 Image-based simulations show important flow fluctuations in a normal left ventricle: what could be the implications? *Ann. Biomed. Eng.* **44** 3346–58

Cigier A, Varray F and Garcia D 2022 SIMUS: an open-source simulator for medical ultrasound imaging. Part II: comparison with four simulators *Comput. Methods Programs Biomed.* **218** 106774

Daae A S, Wigen M S, Fadnes S, Løvstakken L and Støylen A 2021 Intraventricular vector flow imaging with blood speckle tracking in adults: feasibility, normal physiology and mechanisms in healthy volunteers *Ultrasound Med. Biol.* **S0301-5629** 00376–8

Eriksson J, Bolger A F, Ebbers T and Carlhäll C-J 2013 Four-dimensional blood flow-specific markers of LV dysfunction in dilated cardiomyopathy *Eur. Heart J. Cardiovasc. Imaging* **14** 417–24

Eriksson J, Carlhäll C J, Dyverfeldt P, Engvall J, Bolger A F and Ebbers T 2010 Semi-automatic quantification of 4D left ventricular blood flow *J. Cardiovasc. Magn. Reson.* **12** 9–18

Fadnes S, Nyrnes S A, Torp H and Lovstakken L 2014 Shunt flow evaluation in congenital heart disease based on two-dimensional speckle tracking *Ultrasound Med. Biol.* **40** 2379–91

Faurie J, Baudet M, Assi K C, Auger D, Gilbert G, Tournoux F and Garcia D 2017 Intracardiac vortex dynamics by high-frame-rate Doppler vortography—*in vivo* comparison with vector flow mapping and 4D flow MRI *IEEE Trans. Ultrason. Ferroelectr. Freq. Control* **64** 424–32

Faurie J, Baudet M, Poree J, Cloutier G, Tournoux F and Garcia D 2019 Coupling myocardium and vortex dynamics in diverging-wave echocardiography *IEEE Trans. Ultrason. Ferroelectr. Freq. Control* **66** 425–32

Garcia D *et al* 2010 Two-dimensional intraventricular flow mapping by digital processing conventional color-Doppler echocardiography images *IEEE Trans. Med. Imaging* **29** 1701–13

Garcia D 2022 SIMUS: an open-source simulator for medical ultrasound imaging. Part I: theory & examples *Comput. Methods Programs Biomed.* **218** 106726

Garcia D, Saloux E and Lantelme P 2017 Introduction to speckle tracking in cardiac ultrasound imaging *Handbook of Speckle Filtering and Tracking in Cardiovascular Ultrasound Imaging and Video* (Institution of Engineering and Technology)

Gharib M, Rambod E, Kheradvar A, Sahn D J and Dabiri J O 2006 Optimal vortex formation as an index of cardiac health *Proc. Natl Acad. Sci.* **103** 6305–8

Gomez A, Pushparajah K, Simpson J M, Giese D, Schaeffter T and Penney G 2013 A sensitivity analysis on 3D velocity reconstruction from multiple registered echo Doppler views *Med. Image Anal.* **17** 616–31

Gomez A, de Vecchi A, Jantsch M, Shi W, Pushparajah K, Simpson J M, Smith N P, Rueckert D, Schaeffter T and Penney G P 2015 4D blood flow reconstruction over the entire ventricle from wall motion and blood velocity derived from ultrasound data *IEEE Trans. Med. Imaging* **34** 2298–308

Grønli T, Wigen M, Segers P and Lovstakken L 2018 A fast 4D B-spline framework for model-based reconstruction and regularization in vector flow imaging *2018 IEEE Int. Ultrasonics Symp. (IUS). Presented at the 2018 IEEE Int. Ultrasonics Symp. (IUS)* pp 1–9

Günther T and Theisel H 2018 The state of the art in vortex extraction *Comput. Graph. Forum* **37** 149–73

Hansen P C 2000 The L-curve and its use in the numerical treatment of inverse problems *Computational Inverse Problems in Electrocardiology (Advances in Computational Bioengineering)* ed P Johnston (WIT Press) pp 119–42

Hendabadi S, Bermejo J, Benito Y, Yotti R, Fernández-Avilés F, del Álamo J C and Shadden S C 2013 Topology of blood transport in the human left ventricle by novel processing of Doppler echocardiography *Ann. Biomed. Eng.* **41** 2603–16

Jensen J A, Nikolov S, Yu A C H and Garcia D 2016 Ultrasound vector flow imaging: I: sequential systems *IEEE Trans. Ultrason. Ferroelectr. Freq. Control* **63** 1704–21

Kalman D 2009 Leveling with Lagrange: an alternate view of constrained optimization *Math. Mag.* **82** 186–96

Kheradvar A, Houle H, Pedrizzetti G, Tonti G, Belcik T, Ashraf M, Lindner J R, Gharib M and Sahn D 2010 Echocardiographic particle image velocimetry: a novel technique for quantification of left ventricular blood vorticity pattern *J. Am. Soc. Echocardiogr.* **23** 86–94

Leclerc S *et al* 2020 LU-Net: a multistage attention network to improve the robustness of segmentation of left ventricular structures in 2D echocardiography *IEEE Trans. Ultrason. Ferroelectr. Freq. Control* **67** 2519–30

Malm S, Frigstad S, Sagberg E, Steen P A and Skjarpe T 2006 Real-time simultaneous triplane contrast echocardiography gives rapid, accurate, and reproducible assessment of left ventricular volumes and ejection fraction: a comparison with magnetic resonance imaging *J. Am. Soc. Echocardiogr.* **19** 1494–501

Marchese P, Cantinotti M, Van den Eynde J, Assanta N, Franchi E, Pak V, Santoro G, Koestenberger M and Kutty S 2021 Left ventricular vortex analysis by high-frame rate blood speckle tracking echocardiography in healthy children and in congenital heart disease *IJC Heart Vasc.* **37** 100897

Markl M, Kilner P J and Ebbers T 2011 Comprehensive 4D velocity mapping of the heart and great vessels by cardiovascular magnetic resonance *J. Cardiovasc. Magn. Reson.* **13** 1–22

Markl M, Schnell S, Wu C, Bollache E, Jarvis K, Barker A J, Robinson J D and Rigsby C K 2016 Advanced flow MRI: emerging techniques and applications *Clin. Radiol.* **71** 779–95

Martínez-Legazpi P *et al* 2014 Contribution of the diastolic vortex ring to left ventricular filling *J. Am. Coll. Cardiol.* **64** 1711–21

Muth S, Dort S, Sebag I A, Blais M-J and Garcia D 2011 Unsupervised dealiasing and denoising of color-Doppler data *Med. Image Anal.* **15** 577–88

Nahas H, Au J S, Ishii T, Yiu B Y S, Chee A J Y and Yu A C H 2020 A deep learning approach to resolve aliasing artifacts in ultrasound color flow imaging *IEEE Trans. Ultrason. Ferroelectr. Freq. Control* **67** 2615–28

Nucifora G, Badano L P, Dall'Armellina E, Gianfagna P, Allocca G and Fioretti P M 2009 Fast data acquisition and analysis with real time triplane echocardiography for the assessment of left ventricular size and function: a validation study *Echocardiography* **26** 66–75

Nyrnes S A, Fadnes S, Wigen M S, Mertens L and Lovstakken L 2020 Blood speckle-tracking based on high–frame rate ultrasound imaging in pediatric cardiology *J. Am. Soc. Echocardiogr.* **33** 493–503

Onishi T, Saha S K, Delgado-Montero A, Ludwig D R, Onishi T, Schelbert E B, Schwartzman D and Gorcsan J 2015 Global longitudinal strain and global circumferential strain by speckle-tracking echocardiography and feature-tracking cardiac magnetic resonance imaging: comparison with left ventricular ejection fraction *J. Am. Soc. Echocardiogr.* **28** 587–96

Papadacci C, Finel V, Villemain O, Goudot G, Provost J, Messas E, Tanter M and Pernot M 2019 4D simultaneous tissue and blood flow Doppler imaging: revisiting cardiac Doppler index with single heart beat 4D ultrafast echocardiography *Phys. Med. Biol.* **64** 085013

Porée J, Baudet M, Tournoux F, Cloutier G and Garcia D 2018 A dual tissue-Doppler optical-flow method for speckle tracking echocardiography at high frame rate *IEEE Trans. Med. Imaging* **37** 2022–32

Provost J, Papadacci C, Arango J E, Imbault M, Fink M, Gennisson J-L, Tanter M and Pernot M 2014 3D ultrafast ultrasound imaging *in vivo Phys. Med. Biol.* **59** L1–13

Ramalli A, Harput S, Bezy S, Boni E, Eckersley R J, Tortoli P and D'Hooge J 2020 High-frame-rate tri-plane echocardiography with spiral arrays: from simulation to real-time implementation *IEEE Trans. Ultrason. Ferroelectr. Freq. Control* **67** 57–69

Sengupta P P, Pedrizzetti G and Narula J 2012 Multiplanar visualization of blood flow using echocardiographic particle imaging velocimetry *JACC Cardiovasc. Imaging* **5** 566–9

Shahriari S and Garcia D 2018 Meshfree simulations of ultrasound vector flow imaging using smoothed particle hydrodynamics *Phys. Med. Biol.* **63** 1–12

Stugaard M, Koriyama H, Katsuki K, Masuda K, Asanuma T, Takeda Y, Sakata Y, Itatani K and Nakatani S 2015 Energy loss in the left ventricle obtained by vector flow mapping as a new quantitative measure of severity of aortic regurgitation: a combined experimental and clinical study *Eur. Heart J.—Cardiovasc. Imaging* **16** 723–30

Swillens A, Degroote J, Vierendeels J, Lovstakken L and Segers P 2010 A simulation environment for validating ultrasonic blood flow and vessel wall imaging based on fluid-structure interaction simulations: ultrasonic assessment of arterial distension and wall shear rate *Med. Phys.* **37** 4318–30

Töger J, Kanski M, Arvidsson P M, Carlsson M, Kovács S J, Borgquist R, Revstedt J, Söderlind G, Arheden H and Heiberg E 2016 Vortex-ring mixing as a measure of diastolic function of the human heart: Phantom validation and initial observations in healthy volunteers and patients with heart failure *J. Magn. Reson. Imaging* **43** 1386–97

Vixège F, Berod A, Nicoud F, Courand P-Y, Vray D and Garcia D 2021a 3D intraventricular vector flow mapping using triplane Doppler echo *Functional Imaging and Modeling of the Heart, Lecture Notes in Computer Science* ed D B Ennis *et al* (Cham: Springer International Publishing) pp 587–94

Vixège F, Berod A, Sun Y, Mendez S, Bernard O, Ducros N, Courand P-Y, Nicoud F and Garcia D 2021b Physics-constrained intraventricular vector flow mapping by color Doppler *Phys. Med. Biol.* **66** 245019–35

Voorneveld J *et al* 2020 4D echo-particle image velocimetry in a left ventricular phantom *Ultrasound Med. Biol.* **46** 805–17

Zhong Y *et al* 2016 Assessment of left ventricular dissipative energy loss by vector flow mapping in patients with end-stage renal disease *J. Ultrasound Med.* **35** 965–73